Volume 7
Number 8
27 April 2026
Pages 3911–4394

Materials Advances

rsc.li/materials-advances

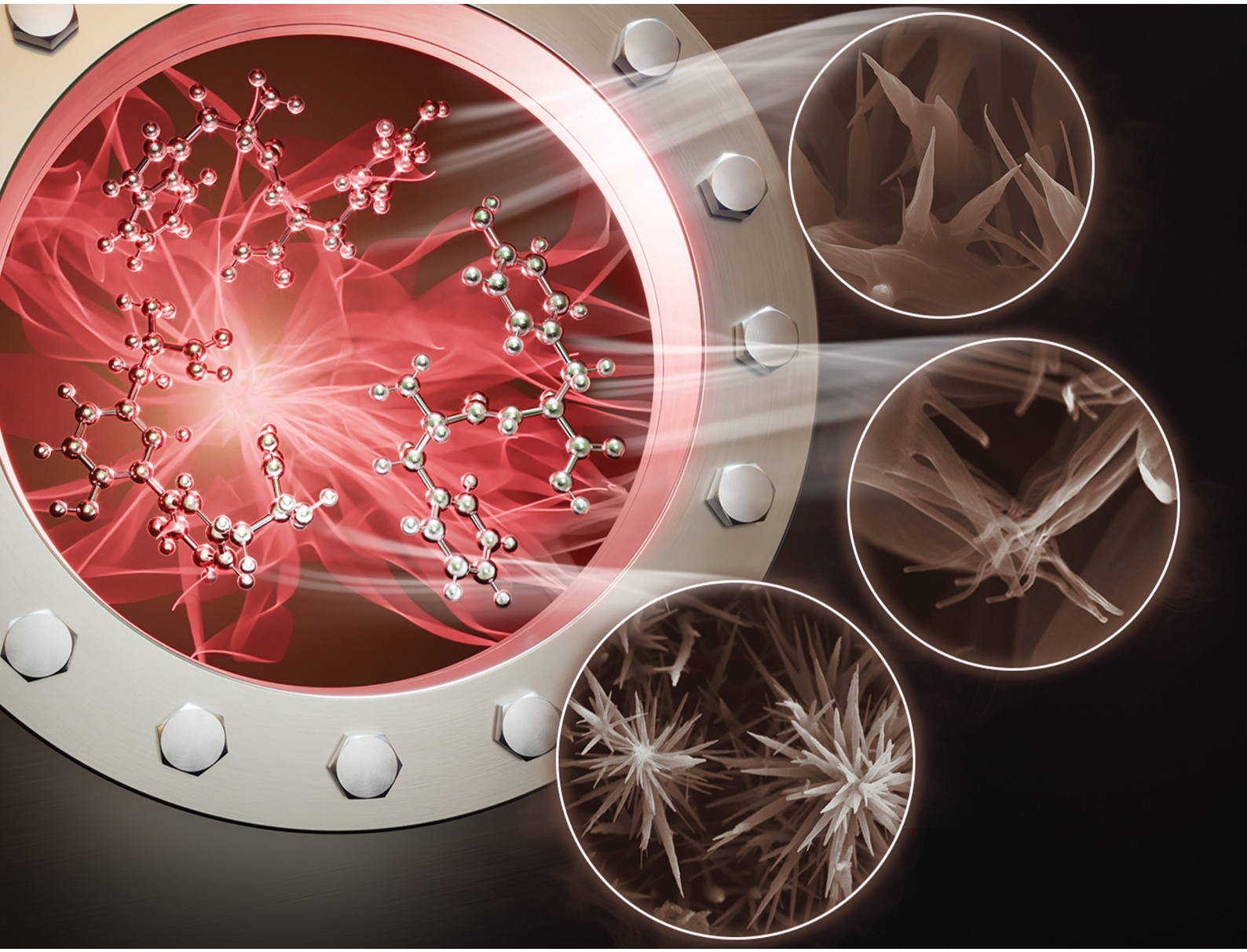

ISSN 2633-5409

ROYAL SOCIETY OF CHEMISTRY

PAPER
Milana C. Vasudev *et al.*
Plasma enhanced vapor deposition of dipeptide nanostructures: nanotubes to nanoflowers

Materials Advances

ROYAL SOCIETY OF CHEMISTRY

PAPER

View Article Online
View Journal | View Issue

Cite this: *Mater. Adv.*, 2026, 7, 4061

Plasma enhanced vapor deposition of dipeptide nanostructures: nanotubes to nanoflowers

Jordan Pagliuca,†[a] Prathyushakrishna Macha,†[ab] Marilyn Naeem[c] and Milana C. Vasudev *[a]

The study of self-assembling peptides for synthesizing nanomaterials is a rapidly growing area in biomedical research. In this study, we report a hybrid deposition technique, plasma enhanced chemical vapor deposition (PECVD), as a reliable method for the synthesis of aromatic tyrosine peptide-based nanostructures with well-defined structural and physicochemical properties. In the custom-built PECVD system, deposition parameters, including the deposition height, substrate tilt, chamber pressure, frequency of plasma pulsation, and presence of physical confinement, were varied, leading to the formation of thin films with desired morphologies, uniformity, and stability. Morphological characterization revealed that the conditions during deposition could be varied to form nanotubular-like structures, whereas higher pressure and the presence of physical confinement led to the emergence of nanoflower-like structures. Nanoflowers are nanostructures with a high surface area-to-volume ratio and a large number of effective sites featuring multilayered porous "petal" structures that extend radially from centralized nucleation sites. Spectroscopic analysis confirmed the simultaneous preservation of peptide chemistry, alterations in the secondary structure, and increased crystallinity, suggesting molecular reorganization. These results provide insights into the plethora of opportunities offered by PECVD for applications in catalytic substrates, regenerative medicine, targeted drug delivery, and the development of antimicrobial coatings.

Received 2nd November 2025,
Accepted 19th February 2026

DOI: 10.1039/d5ma01273b

rsc.li/materials-advances

1. Introduction

Self-assembling biological macromolecules, such as peptides, proteins, and DNA, have been utilized as polymeric materials, nanoparticles, vesicles, fibers, and hydrogels. These materials can bridge the gap in biological applications, such as biosensors, biocompatible scaffolds, and implant coatings, and can also be utilized in bioelectronic applications, photovoltaic cells, and templating platforms. Peptides are of particular interest owing to their versatility and composition. Peptides can self-assemble in a complex, hierarchical manner, where their interactions result in nanoscale or microscale structures.[1,2] These highly organized structures have unique functional properties such as high aspect ratios, semi-conductivity, crystallinity, and stiffness.[3–5] Controlled fabrication of 3D self-assembled architectures over large surface areas is a promising candidate for catalysis, biosensing, and biomedical applications such as tissue scaffolds. The self-assembly of peptides in solutions has been limited to 1D assemblies; however, the ability to produce complex 2D and 3D architectures is useful for fabricating multifunctional materials.[6] In this study, we report the 2D and 3D assembly of vertically oriented thermally stable nanostructures composed of aromatic tyrosine-based dipeptides *via* plasma-enhanced chemical vapor deposition (PECVD). Redox-active amino acids, such as tyrosine and tryptophan, have been used as precursors for nanostructure formation using plasma enhanced chemical vapor deposition.[7]

Tyrosine is a redox-active amino acid owing to its phenolic groups, which can undergo oxidation and reduction.[8,9] The electronic and proton conductivities are highest in tyrosine-rich peptides, as observed in our preliminary studies and the published literature, leading to a growing interest in tyrosine-based biomaterials.[7,10–12]

Chemical vapor deposition (CVD) is a method that eliminates some of the issues faced by wet chemical synthesis, using single-step dry fabrication to provide better control of coverage, uniformity, and stability.[13,14] CVD is widely used for the deposition of inorganic materials, which have multiple applications in flat-screen panel displays, solar cells, and semiconductor devices.[15–17] CVD is less commonly used in the deposition of non-traditional monomers, such as peptides, which cannot sustain the high temperatures of deposition. Hybrid techniques, such as PECVD, have been used for the deposition of inorganic and

[a] *Department of Bioengineering, University of Massachusetts Dartmouth, Dartmouth, MA 02747, USA. E-mail: mvasudev@umassd.edu*
[b] *Molecular Devices, Danaher, San Jose, CA 95134, USA*
[c] *Department of Chemistry and Biochemistry, University of Massachusetts Dartmouth, Dartmouth, MA 02747, USA*
† Prathyushakrishna Macha and Jordan Pagliuca contributed equally to this study.

organic thin films and even inert precursors.[18–20] The low temperature required for deposition in the plasma-assisted deposition process and the precise control of reaction parameters are advantageous for the self-assembly of both biological and biomimetic molecules, as there is a decreased risk of biodegradation.[21,22] PECVD facilitates thin film deposition through plasma-mediated radical generation from precursor molecules and substrate activation induced by plasma.[18,23] In this study, PECVD enabled the synthesis of peptide-based nanostructures by combining plasma-induced radical chemistry with molecular self-assembly. Complex non-covalent interactions during the deposition process, including hydrogen bonding, electrostatic interactions, and π–π stacking, led to the 2D and 3D assembly of the nanostructures observed in this study.[2,24] The precursors are either in their liquid, solid, or gas phases that undergo thermal vaporization and are then induced into the plasma stream for deposition. The argon gas plasma used in this study was generated through radio frequency (RF) excitation (13.56 MHz), which causes ionization and dissociation reactions in the gas, producing ions, neutral species and reactive radicals. In addition to increased reactivity, PECVD provides additional control over crosslinking and surface chemistry and retains the functional groups of the starting precursors during deposition.[25–27] Aromatic dipeptides such as WY, FY, and YY were sublimed into a low-pressure argon plasma, where energetic electrons and ions fragment the molecules and activate the substrate surface. This initiates radical recombination, forming a crosslinked seed layer that retains functional groups such as amides and phenols under mild plasma conditions.[28] Following deposition, the non-covalent interactions intrinsic to the dipeptides guide further organization. Hydrogen bonding between the backbone amides and π–π stacking among the aromatic rings promote lateral packing and curvature, leading to anisotropic morphologies such as hollow nanotubes. These interactions are entropically favored and have been shown to drive hierarchical assembly in tyrosine-based systems.[29,30] The thermal energy of the plasma can induce the cyclization of linear dipeptides into diketopiperazine rings, enhancing structural stability. Spectroscopic analyses confirm water loss and the formation of new amide bonds during this process, indicating cyclization and improved molecular packing.[6] Additionally, limited oxidation of tyrosine side chains generates phenoxy radicals that couple covalently, reinforcing the structure without disrupting supramolecular organization.[27] The resultant thin films exhibit durability, chemical inertness, and resistance to mechanical wear.[31]

Variation of the process parameters allows for the formation of an assortment of unique and morphologically distinct vertically aligned nanostructures, ranging from nanotubes, nanoflowers, nanorods, and even nanohelices.[6] Nanoflowers are one such configuration of nanostructures that have garnered attention in recent years owing to their comparatively high surface area-to-volume ratio and large number of effective sites.[32] These hierarchical structures exhibit floral-like morphologies characterized by nested three-dimensional architectures featuring multilayered porous ''petal'' structures that extend radially from centralized nucleation sites. The operational simplicity and cost-effectiveness of PECVD synthesis enable the utilization of diverse precursor chemistries, facilitating the formation of organic, inorganic, and hybrid nanoflower architectures.[33,34] Optimization of the deposition conditions, including deposition time, temperature, and precursor concentration, is required to synthesize nanoflowers with unique sizes and structures. Although a few studies have reported nanoflower synthesis using exclusively organic precursors, the self-assembly mechanisms and functional implications of such nanostructures remain inadequately characterized.[35,36] The proposed mechanism for assembly begins with the coordination of the amide groups of the organic (amino acid) components, forming nucleation centers for the aggregation of primary nanostructures, and subsequently, petal-like nanoflower morphology due to spontaneous self-assembly during deposition. The resulting nanoflower morphology, whether compact (nascent) or branched (mature), is predominantly dictated by the initial peptide precursor concentration. The precursor concentration exhibited a direct correlation with the number and geometry of the primary nanostructures formed during nucleation, thereby influencing the molecular diffusion. Higher precursor concentrations and geometric constraints on the substrate surface affect the rate of aggregation and intermolecular collision frequencies, resulting in more densely packed and compact structures.

2. Results and discussion

PECVD is a highly versatile deposition methodology in which multiple process variables can be controlled to achieve the specific morphological and structural characteristics of the resultant thin films. To understand the influence of the processing conditions on nanostructural morphology and thermodynamic stability, critical deposition parameters such as chamber pressure, RF power, argon carrier-gas flow rate, deposition time, substrate orientation, evaporator-substrate spacing, geometric constraints on the substrate, and amount of peptide were manipulated in this study (SI Fig. S1 and Table S1). Given the large number of available parameters, specific process variables such as the duty cycle, RF power, and argon flow rate were held constant throughout the experimental matrix. The parameters that were varied included the height of the substrate holder, pressure set point, RF power frequency, presence of geometric constraints, and tilt angle (substrate orientation). Temperature plays a crucial role in the deposition of dipeptides using PECVD, influencing both vaporization kinetics and cyclization reactions. Determining the characteristic temperature, also known as the glass liquid transition phase temperature, at which peptides undergo condensation polymerization to form thermodynamically stable cyclic conformations, is important for successful deposition. DSC and TGA analyses were performed to measure the phase changes as a function of temperature and to assess the temperatures at which the precursors underwent a glass-liquid transition. The DSC data for the tryptophan–tyrosine (WY) linear dipeptide (Fig. 1A) indicated the onset of a phase change at approximately

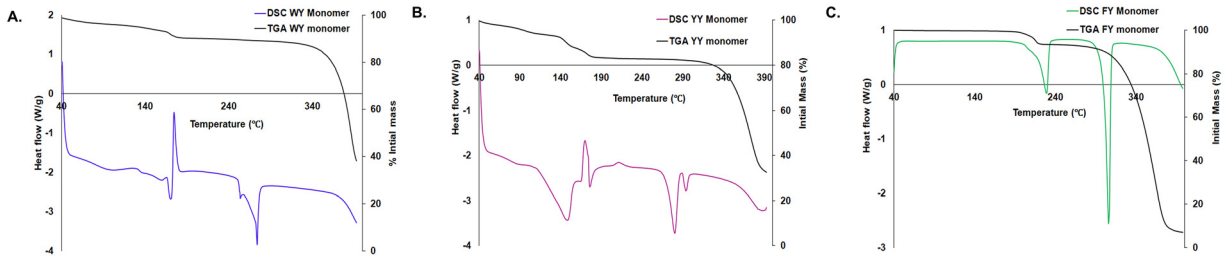

Fig. 1 DSC and TGA thermograms of WY (A), YY (B), and FY (C) linear monomers demonstrating the phase change and melting temperatures.

170 °C. An exothermic cold crystallization peak was observed at ~175 °C, indicating crystallization. The dityrosine (YY) monomer exhibited a thermal transition trend similar to that of the WY monomer (Fig. 1B). Following the initial onset of the phase change (150 °C), cold crystallization reactions were observed as exothermic peaks at 170 °C. The heat flow out of the sample suggests the release of excess free energy from the monomers, allowing the arrangement of the molecules into ordered structures. As the temperature increased, energy flowed into the sample, manifested as endothermic melting peaks at 280 °C and 294 °C. The recorded transition temperature for phenylalanine–tyrosine (FY) monomers was slightly elevated, with the initial onset of phase change at 170 °C and endothermic peaks at 230 °C and 295 °C (Fig. 1C). A significant exothermic peak similar to those of WY and YY was absent in the FY monomer, although a minimal peak was observed at 201 °C. The TGA observations were consistent with DSC data. Significant weight loss due to dipeptide decomposition occurred at approximately 355 °C for WY and YY and 359 °C for FY linear monomers. The sublimation temperatures used in the PECVD deposition of the dipeptides were based on the temperatures determined using DSC. The deposition of the WY peptide at temperatures much higher than the cold crystallization transition led to the formation of deformed nanostructures with beads owing to the expansion and bubbling of previously formed structures (SI Fig. S2). The key elements of molecular self-assembly are non-covalent interactions, which lead to chemical complementarity and structural compatibility. To assess the impact of PECVD on the thermostability of the resulting nanostructures, DSC was performed after the deposition. The absence of exothermic peaks in all samples was a positive indicator of the complete crystallization of the monomer into ordered structures, and no changes were observed in the degradation temperature (SI Fig. S3). Dipeptide building blocks form hierarchical structures upon vaporization onto a substrate held at room temperature. Non-covalent interactions, such as π–π stacking between the aromatic benzene rings of the dipeptides and hydrogen bonding involving amine (N–H) and carboxyl groups, are involved in this process.

Peptides undergo cyclization during vaporization, accompanied by the loss of a water molecule, as confirmed by ultra-performance liquid chromatography-mass spectrometry (UPLC-MS) measurements (SI Fig. S4). Ultra-high-performance liquid chromatography (HPLC) was employed to identify changes in the molecular weight of the dipeptide monomer and PECVD-deposited samples (Waters Inc., UHPLC-QTOF MS, Agilent). The retention times obtained by HPLC for the peptide monomers and PECVD-deposited samples indicate changes in the peptide structure, following PECVD deposition. The PECVD WY nanostructures and cyclic dipeptide monomer both exhibited a retention time of 2.20 min, and the linear WY monomer eluted at approximately 2.05 min (Fig. 2A). The linear FY monomer and PECVD FY nanostructures had retention times of 2.1 min and 2.20 min, while the YY monomer and PECVD YY nanostructures eluted at 2.02 min and 2.13 min, respectively (Fig. 2B and C). While the peak shape and area remained constant, the small shift in the retention times of the PECVD-deposited samples was consistent with the behavior of the cyclic monomers, as observed in the WY cyclic peptide monomer.

Scanning electron microscopy (SEM) was the primary tool used for the morphological characterization of the thin films deposited under varying conditions, enabling the analysis of

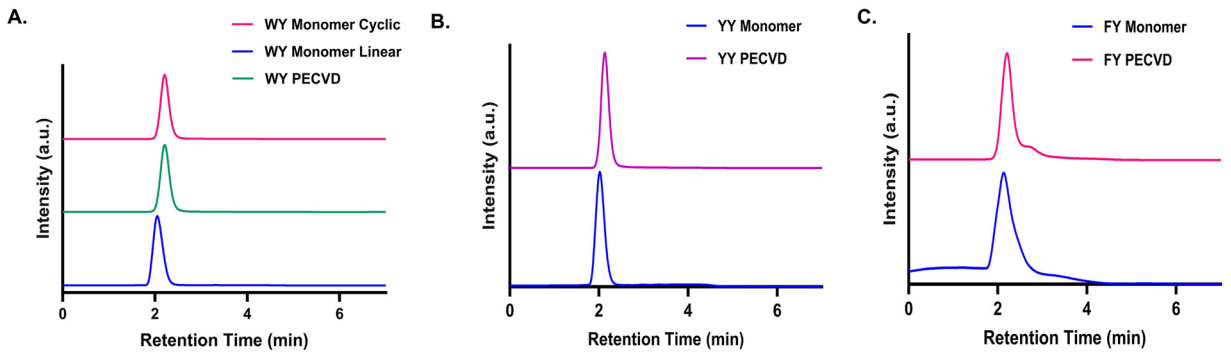

Fig. 2 HPLC chromatograms of the dipeptide monomers and PECVD-deposited nanostructures for WY (A), YY (B), and FY (C).

the surface topography, dimensions, and nanostructural features of the hierarchical structures. As previously observed with diphenylalanine depositions, peptide deposition begins with a thin seeding layer with no discernible morphology, which then branches outward from the seed layer to form tubes, rods, or other morphologies.[6] One of the crucial parameters during peptide deposition is the height of the substrate (from the evaporator), and increasing the distance of the substrate affects the thin film formation. The distance between the substrate and evaporator was incrementally changed in steps of 1 mm from 2–7 mm (Fig. 3a–c). 4–5 mm was consistently optimal for consistent deposition across all dipeptide compositions. All other heights considered were suboptimal, with no observable deposition when the distance was too high or the formation of layered structures when the substrate was at very short distances from the evaporator. Subsequently, the substrate orientation was adjusted through controlled angular changes, with the tilt angles systematically varied to investigate the influence of substrate positioning on the film deposition kinetics and the resultant morphology. The substrate was tilted with respect to the evaporator and tested at tilt angles ranging from 0° to 45°, while holding all other parameters constant. The primary observation was that the morphology of the structures changed drastically between rods and tube-like morphology to ribbons. Ultimately, conical stepped structures were observed predominantly in the FY depositions, leading to the conclusion that the tilt angles and composition of the dipeptides led to different configurations (Fig. 3d–f). The effects of the

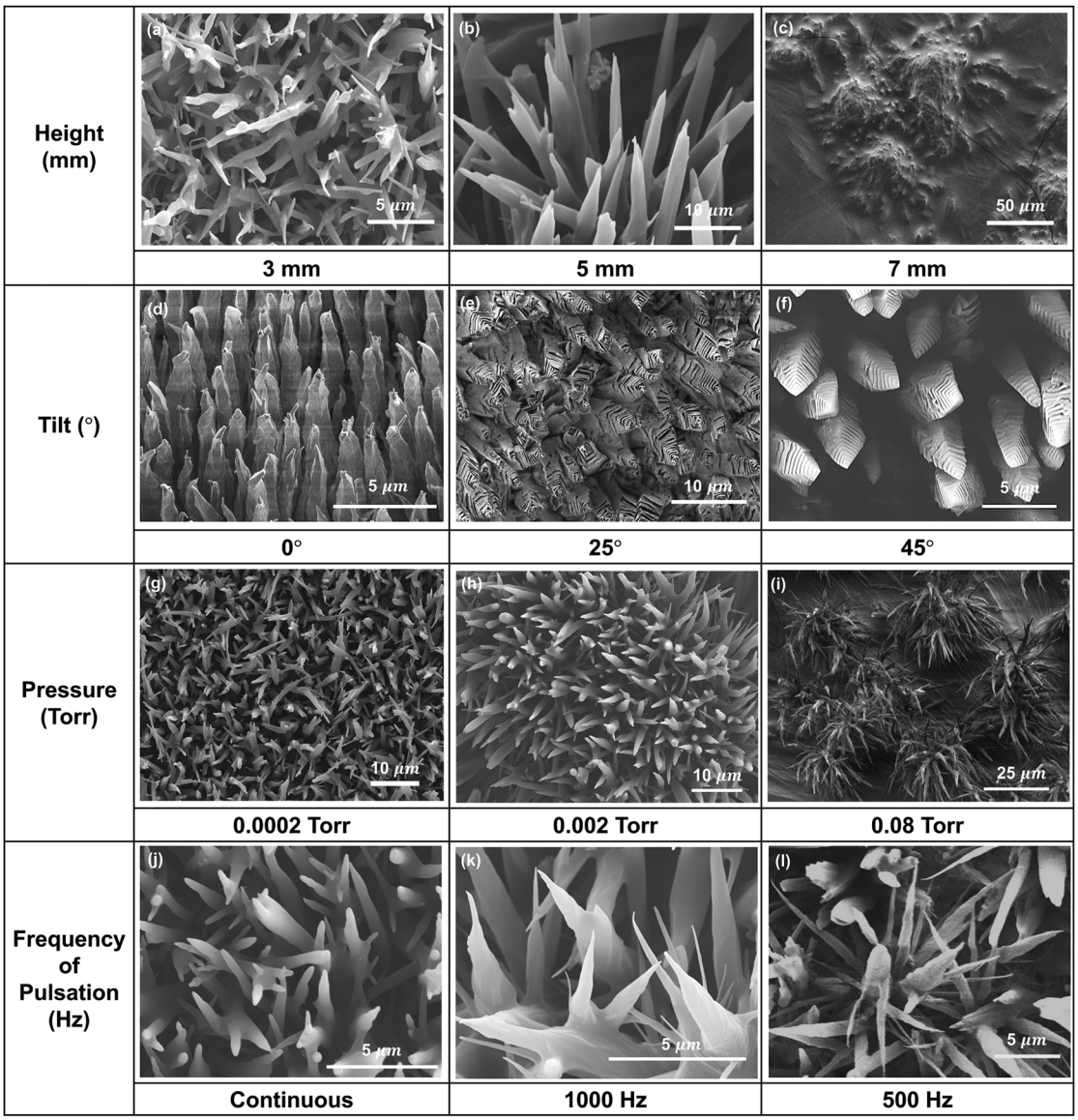

Fig. 3 SEM micrographs of PECVD-deposited WY dipeptide nanostructures synthesized under different conditions. The height of deposition was in the range of 3–7 mm (a)–(c), tilt angle was tested from 0–45° (d)–(f), chamber pressure varied in a range of 0.0002–0.08 Torr (g)–(i), and frequency of plasma pulsation was either held constant (j) or tested at 1000 Hz (k) or 500 Hz (l).

deposition time were tested in increments of 5 min, within a range of 5–15 minutes.

Increasing the deposition time prompted the lengthening of the nanorods/tubes, but beyond 20 min, this led to deformation (SI Fig. S5). At the lowest deposition time of 5 min, the rods or tubes were shorter and had disorganized morphologies. After 10 min, the structures began to appear as rod-like or tubular. At the longest deposition time of 15 min, rod- and tube-like structures were frequently observed. The presence of a butterfly valve with predetermined set points controlled the pressure in the vacuum chamber. The depositions were performed at higher pressure settings of 0.08 Torr as well as lower pressures of 0.008–0.0002 Torr and were compared (Fig. 3g–i). Lower pressure slowed the deposition process, resulting in the samples becoming less chaotic, straighter, and with fewer deformities than those deposited at higher pressures. Higher-pressure conditions led to the formation of a clustered floral morphology (Fig. 3i). The RF power was pulsed and evaluated across the peptides at three different frequencies: continuous, 1000 Hz, and 500 Hz, at a constant duty cycle of 25%, while the power for all depositions was maintained constant at 30 W. Power modulation was achieved using a pulse generator, where the duty cycle is a fraction of the total time the power is applied [DC = $T_{on}/(T_{on} + T_{off})$]. The frequency affected the macroscopic chirality of the individual nanostructures. Continuous plasma frequency structures exhibited achiral structures, whereas lowering the frequency to 1000 and 500 Hz demonstrated macroscopic chirality, particularly at the tips of the deposition (Fig. 3j–l). Considering all the deposition parameters tested and the resulting morphological observations, a 5 mm height, 15 sccm argon flow, 5 mg peptide weight, 0° tilt, 10 min of deposition time, and 0.0004 Torr pressure were used to produce nanotube/rod-like arrangements, as opposed to nanoflower morphologies. Replicating these conditions confirmed the consistent formation of uniform, stable, morphologically accurate, and evenly distributed structures across all samples. To further demonstrate that the modification of these parameters can be exploited to produce nanostructures with varying morphologies, we utilized physical constraints such as TEM grids and other metallic mesh (205–125 μm width copper mesh) attached to the substrate used for deposition. The resulting alignment of the peptide monomers produced spread-out nanoflower-like morphologies. Fig. 4 shows the deposition of all the dipeptides, resulting in varying nanoflower-like morphologies in the presence of the TEM grid used as a physical constraint on the substrate.

Fourier-transform infrared (FTIR) and Raman spectroscopy were employed to obtain spectral data indicating potential chemical and structural differences in the peptide-based nanostructures following PECVD deposition (Fig. 5A and B). In PECVD deposited dipeptides, peaks designating H-bond donor groups (C–H, C═C, C═O, N–H, and O–H) are of particular interest because of their well-established role in driving self-assembly processes through various non-covalent interactions (van der Waals, hydrogen bonds, and London dispersion forces). Deconvolution of the 1500–1800 cm^{-1} region for the three

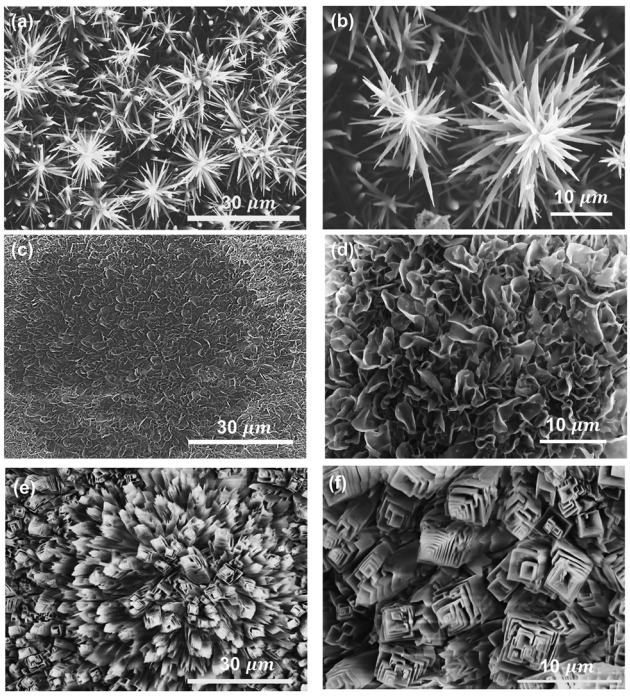

Fig. 4 SEM micrographs of WY (a) and (b), YY (c) and (d), and FY (e) and (f) PECVD-deposited nanostructures produced in the presence of confinement, indicating the structural dependency on the dipeptide composition.

dipeptides (Fig. 5D–F) helped identify the peaks which an important role in the Amide I and II region. The Amide I band (~1500–1580 cm^{-1}), demonstrating one major peak for all deposited dipeptide combinations at ~1517 cm^{-1}, indicative of a C═O connected carbon symmetrical vibration. A distinct peak in the Amide II region was observed at ~654 cm^{-1} (FY)–1667 cm^{-1} (WY and YY), consistently across all the deposited peptide samples (SI Fig. S6). This value indicates that PECVD-deposited peptide nanostructures have a predominantly α-helical backbone conformation in FY nanostructures and β-turn/loops (~1667 cm^{-1}) both in WY and YY nanostructures. While dipeptides are too short to form true α-helices or β-sheets, this feature observed in the assembled nanostructures likely reflects intermolecularly hydrogen-bonded conformations consistent with localized backbone ordering.[37,38] This suggests that there is localized ordered motifs dominated by turn-like conformations as well as some aggregated β-strand-like interactions. This is consistent with small, ordered fibrillar segments in the assembled nanostructures rather than classical long α-helices.[39] The similarity between these amide peaks and those previously reported in oven-cyclized, solution-phase self-assembled nanotubes indicates the occurrence of cyclization during the sublimation of the dipeptides onto the substrate.[40] Cyclization also accounts for the presence of a primary amine and a small –OH peak in the range of ~3200–3500 cm^{-1}. The broad, peaks centred around 3178–3185 cm^{-1} in the amide A region indicate the hydrogen bonded N–H and could also have a contribution from structurally bound water. The sharp peaks at ~3536 cm^{-1} observed in the FY PECVD deposited samples and notably absent in the monomers is consistent with free –OH

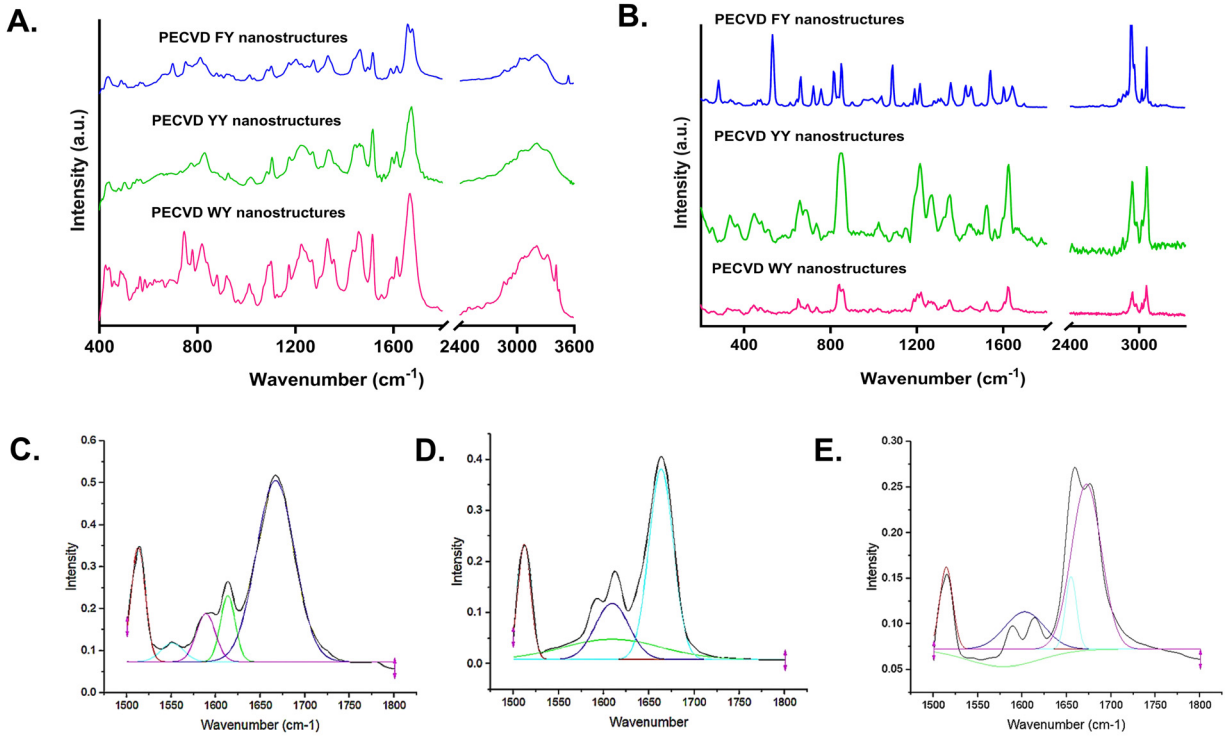

Fig. 5 FTIR (A) and Raman (B) spectral analysis of WY, YY, and FY PECVD-deposited peptide nanostructures; deconvoluted FTIR spectra in the amide I region for WY (C), YY (D), and FY (E) PECVD-deposited peptide nanostructures.

groups indicating adsorbed water. The peak at 3417 cm^{-1} in WY samples is characteristic of the N–H stretching in indole ring of tryptophan residues. Analysis of the Amide III spectral band ($\sim$1200 cm^{-1}–1350 cm^{-1}) indicates localized backbone ordering consistent with α-helices with a minor contribution from unordered and random structures in all the dipeptide nanostructures, displaying noteworthy peaks centered around 1330 cm^{-1} and 1275 cm^{-1}, respectively. Unique to WY nanostructures, there is a strong peak at $\sim$1220 cm^{-1} that may originate from side-chain interactions or local hydrogen-bonding, as no accompanying Amide I peak at $\sim$1620 cm^{-1} characteristic of extended β-sheet structures was observed.

Raman spectroscopy indicated scattering peaks characteristic of tyrosine residues with doublets observed in the range of 830–850 cm^{-1} (I856/830 >1) linked to the Fermi resonance phenomenon (Fig. 5B).[41] In the lower frequency regions ($\sim$1200 cm^{-1}–1350 cm^{-1}), there is also evidence of many prominent peaks attributed to the aromatic residues of tryptophan, tyrosine, and phenylalanine.[41] Doublet signatures in the C–H stretching region were observed at $\sim$2936 and 3065 cm^{-1} for the WY, YY, and FY PECVD deposited samples. The N–H and O–H stretching peaks, typically observed in dipeptide Raman signatures at approximately 3200–3300 cm^{-1} and $\sim$3300–3500 cm^{-1}, respectively, were negligible in all PECVD-deposited samples. In the Amide III band spectral region (1200–1350 cm^{-1}), singular peaks were identified at $\sim$1220 cm^{-1} for WY and YY, whereas the peak for FY was localized at $\sim$1215 cm^{-1}. Analysis of the amide I bands further reflected the atoms of the peptide backbone, ranging from $\sim$1600 to 1800 cm^{-1}. A dominant peak in the WY sample, centered at approximately 1620 cm^{-1}, which is characteristic of extended β-sheet structures, was observed. The α-helical-ascribed peaks were right-shifted and dominated the remnant spectra, with FY peaking at 1641 cm^{-1} and YY peaking at 1633 cm^{-1}. Associated with N–C stretching, skeletal stretching, and N–H bending vibrations, these two-amine group-linked regional nuances suggest the influence of these bonding patterns on protein folding and, thus, nanostructure self-assembly.

The molar ellipticity measurements in the circular dichroism (CD) spectra agreed with the conformational trends observed in the FTIR and Raman spectroscopy for the PECVD deposited WY, FY, and YY nanotubes. The analysis was conducted using Dichroweb software with the Contin-LL and K2D packages.[42–47] Both the FY and YY nanotube spectra display two distinct minima at approximately 203 and 222 nm and 208 and 228 nm, respectively (Fig. 6D).[48] The FY assembled nanostructures also demonstrate a strong positive peak at 190 nm absent in the other two peptides. The strong negative peak at wavelength of 203–208 nm is attributed to π–π* transitions and the peak at 220–228 nm is attributed to n–π* transition.[49,50] While these features are commonly associated with α-helical structures in proteins, in short dipeptide assemblies, they are more likely attributed to local backbone ordering and hydrogen bonding between closely packed peptide and aromatic residues. The short peptide length inhibits the formation of true α-helices, and the observed CD pattern arises from chiral supramolecular packing and electronic interactions among neighboring amide and aromatic residues that mimic helical

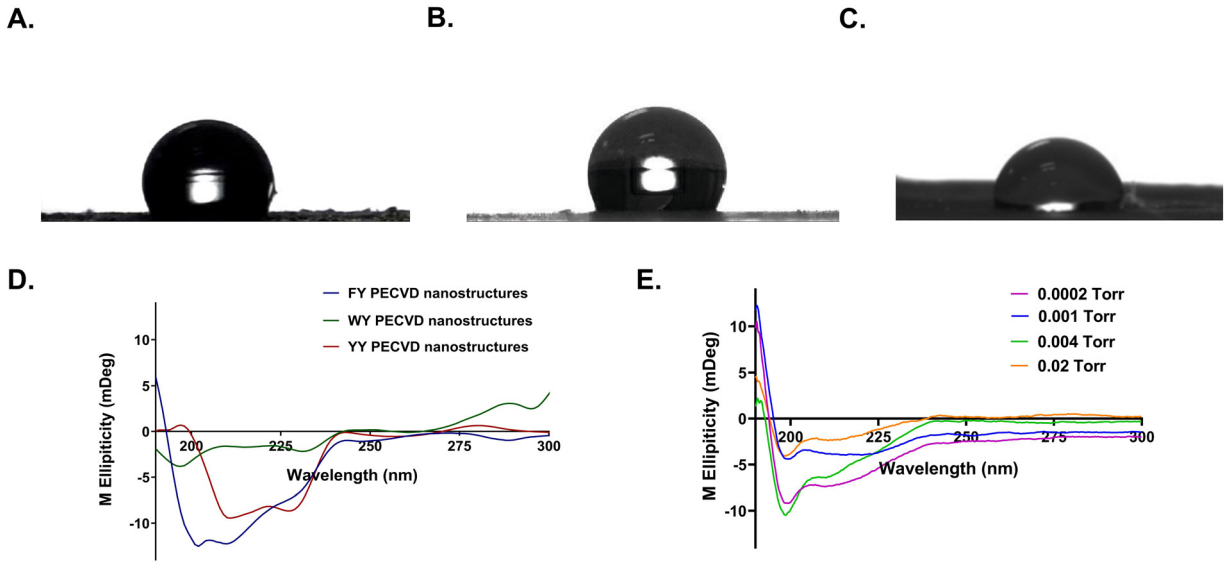

Fig. 6 Contact angle images WY (A), YY (B), and FY (C) PECVD deposited peptide nanostructures; CD spectral analysis of PECVD deposited peptide nanostructures across differing dipeptide compositions (D) and pressure set points (E). For pressure set point analysis, FY was used as the representative dipeptide.

signatures. WY nanotubes alternatively reveal minimal α-helical like contributions but equally strong populations of β-strand like (minima at 216 nm), β-turn like (minima at 232 nm), and random coiled structures (minima at 200 nm), consistent with mixed or aggregated conformations.

The structural conformation of PECVD-deposited nanostructures is similar to that predicted by other synthesis methods, solution-phase self-assembly, and computer simulations. We also investigated how variations in the deposition conditions influenced the conformation of FY nanostructures to understand the impact of processing parameters beyond dipeptide composition. FY nanostructures were deposited at four pressure set points: 0.0002, 0.004, 0.001, and 0.02 Torr (Fig. 6E). All four conditions tested exhibited two minima, with the first at approximately 200 nm and the second in the range of 210–220 nm. This spectral pattern is characteristic of α-helical conformations, where double minima are observed at ∼208 and ∼222 nm. Therefore, the flattening of the spectra around 222 nm may suggest partial or reduced helicity due to the PECVD process parameters. The primary difference between the deposition conditions was observed at ∼191 nm, where a positive peak was observed for all four samples at different intensities. The intense positive peak at ∼190 nm corresponds to π–π* transitions, further supporting the potential for helical-folded conformations.[51] At the lowest pressure setting of 0.0002 Torr, the CD spectrum revealed distinct negative minima, accompanied by a strong positive maximum near 190 nm. At 0.001 Torr, the intense positive peak near 190 nm is present, whereas the negative minima had reduced intensity and increased broadening at longer wavelengths. This may indicate a partial disruption of the α-helical content and a transition toward less ordered structures, possibly including random coil and β-turn motifs. At 0.004 Torr, the positive peak at 190 nm is present but at much lower amplitude and negative bands are absent at longer wavelengths, consistent with the loss of ordered helices and an increase in random coil structures. This spectral signature is typical of unfolded or partially aggregated peptide states, in which the characteristic α-helical minima disappear. At the highest pressure set point of 0.02 Torr, the CD signal flattened substantially, with a minor positive peak near 190 nm at and an almost absent negative band at higher wavelengths, indicating a predominantly disordered or random coil state with a minimal secondary structure. These findings suggest that pressure set-points during the deposition influences the degree of molecular ordering, with higher deposition pressures leading to reduced organization and increased disorder, transitioning from α-helices at lower pressures to disordered conformations at higher pressures.

The surface wettability of the self-assembled peptide nanostructures was assessed through water contact angle (θ) (WCA) measurements (Fig. 6A–C). These were acquired using the sessile drop method on a Ramé-Hart Goniometer with a precision of $\pm$ 0.1°. In this study, samples with a WCA greater than or equal to 90.0° were categorized as hydrophobic. All PECVD-deposited nanostructures displayed hydrophobic properties, with WCA values of 104.6 $\pm$ 6.3° (FY), 109.0 $\pm$ 6.2° (WY), and 120.9 $\pm$ 3.5° (YY), with YY exhibiting the highest hydrophobicity across all samples. The effect of this synthesis method was consistent with previously reported hydrophobicity indices for Trp, Tyr, and Phe.[52] XRD analysis of the deposited structures was performed to assess the crystallinity and molecular organization of the peptides. The comparative XRD data revealed the critical role of the aromatic dipeptide composition in supramolecular ordering and crystallinity. Collectively, the diffraction patterns revealed highly crystalline and distinct molecular packing signatures, with varying crystallinity levels across different dipeptides (Fig. 7). The YY nanostructures exhibited a prominent low-angle peak corresponding to a

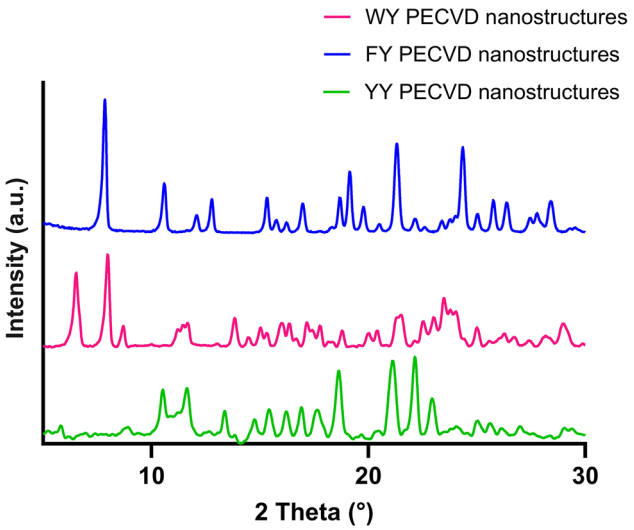

Fig. 7 XRD spectra of WY, YY, and FY PECVD-deposited peptide nanostructures.

d-spacing of ≈7.8 nm along with some well-resolved intermediate and higher-angle peaks indicating *d* ≈13 to 2.5 Å. Some of these peaks can be attributed to the nanotube wall thickness/diameter, backbone organization, and aromatic π–π stacking. The presence of two tyrosine residues promoted strong aromatic interactions and hydrogen bonding; however, the broadening of some diffraction peaks indicated the effect of the PECVD process parameters, whereas the solution-phase-synthesized nanotubes demonstrated strong crystalline peaks in comparison (SI Fig. S7).

The spectra of the PECVD WY nanostructures exhibited moderate crystallinity with an ordered packing arrangement, and the dimensions of the structures resembled those of YY, showing a similar low-angle peak near a *d*-spacing of approximately 8.3 nm. The remnant intermediate- and higher-angle peaks, particularly between *d* ≈ 10.9–3.6 Å, were broader and less intense. Substituting tryptophan for the secondary tyrosine residue may reduce the efficiency of π–π stacking and hydrogen bonding through steric bulk, leading to a looser molecular packing. The FY nanotubes exhibited the highest crystallinity in both the solution and PECVD nanostructures, which was supported by the intensity and sharpness of the diffraction peaks (SI Fig. S7). By a small margin, these nanotubes had the largest diameter of all dipeptides, with a *d*-spacing of ∼8.5 nm. Intermediate and high-angle peaks with *d*-spacing of ∼11.06–7.19 Å reflect short-range ordering. The substitution of phenylalanine in place of the secondary tyrosine residue contributes to stronger aromatic interactions and hydrogen bonding. The highly crystalline and tightly packed FY PECVD nanostructures differ slightly from those of the WY and YY PECVD nanostructures, which are crystalline but could be more loosely organized, correlating with their expected intermolecular interactions.

^{1}H NMR spectroscopy of the dipeptide monomers (WY, YY, and FY) and PECVD-deposited nanostructures was performed to elucidate the spectral changes reflecting chemical transformations during nanotube formation (Fig. 8). The monomer and nanostructure samples were solubilized at a concentration of 10 mg mL^{-1} in DMSO-d_6, and the resulting spectra, particularly in the aromatic (6.0–8.0 ppm) and aliphatic regions (2.5–3.5 ppm) regions, were compared. Residual resonance signals at approximately 3.3 ppm and 2.5 ppm were attributed to remanent H_2O and DMSO, whereas the range of 0.5 ppm to 2.4 ppm was attributed to residual peptide. Across all samples, characteristic aromatic proton signals linked to tyrosine residues were conserved, indicating retention during PECVD deposition. The WY monomer exhibited distinctive –OH and indole –NH signals at 10.96 and 8.33 ppm, respectively, alongside other aromatic resonances observed between 7.63 and 6.55 ppm. Following PECVD deposition, the resulting nanostructures produced similar signals with slight shifts and additional –NH resonances observed at δ 9.15, 7.82, and 7.63 ppm. In the aliphatic region, the WY nanostructures also display variations in splitting patterns, which may be attributed to increased hydrogen bonding, backbone, or side-chain modifications consistent with polymerization. The YY monomer spectrum demonstrated aromatic resonances between 7.02 and 6.65 ppm, with one –NH signal at 8.19 ppm. These signals were slightly shifted following deposition, along with the emergence of new downfield –OH signals at 9.22 ppm, suggesting a structural reconfiguration mechanism that introduced hydroxylated groups into the structure. Various splitting patterns were observed in the aliphatic region of the deposited YY nanostructures. The aromatic region of the FY monomer shows the presence of aromatic protons between 7.31 and 6.62 ppm, along with a distinctive –NH peak at 8.61 ppm. Similar to the previous dipeptide combinations, the FY nanostructures produced following PECVD deposition had new downfield –OH signals at 9.21 ppm, broadening patterns of –NH/aromatic signals, and varied splitting patterns in the aliphatic region. Collectively, these modifications in the FY dipeptide were consistent with increased hydrogen bonding and the formation of nanostructured polymer networks. Overall, the ^{1}H NMR spectral differences suggest chemical modifications that give rise to nanostructures across WY, YY, and FY monomers, followed by the PECVD deposition.

3. Conclusions

The evolution of PECVD has enabled the controlled deposition of peptide-based bionanomaterials. This efficient process eliminates the need for solvents and elevated temperatures, simplifying the self-assembly process and reducing the risk of monomer degradation.[6,53] In this study, we report the formation of highly stable, stiff, high-aspect-ratio dipeptide coatings with the ability to control the morphological structure and material properties. During PECVD, plasma polymerization proceeds *via* random radical recombination mechanisms initiated by the generation of reactive radicals from precursor molecules within the plasma environment. The polymerization process begins with the formation of radicals through precursor fragmentation, followed by a chain propagation reaction. The persistence of radical sites along the polymer chains

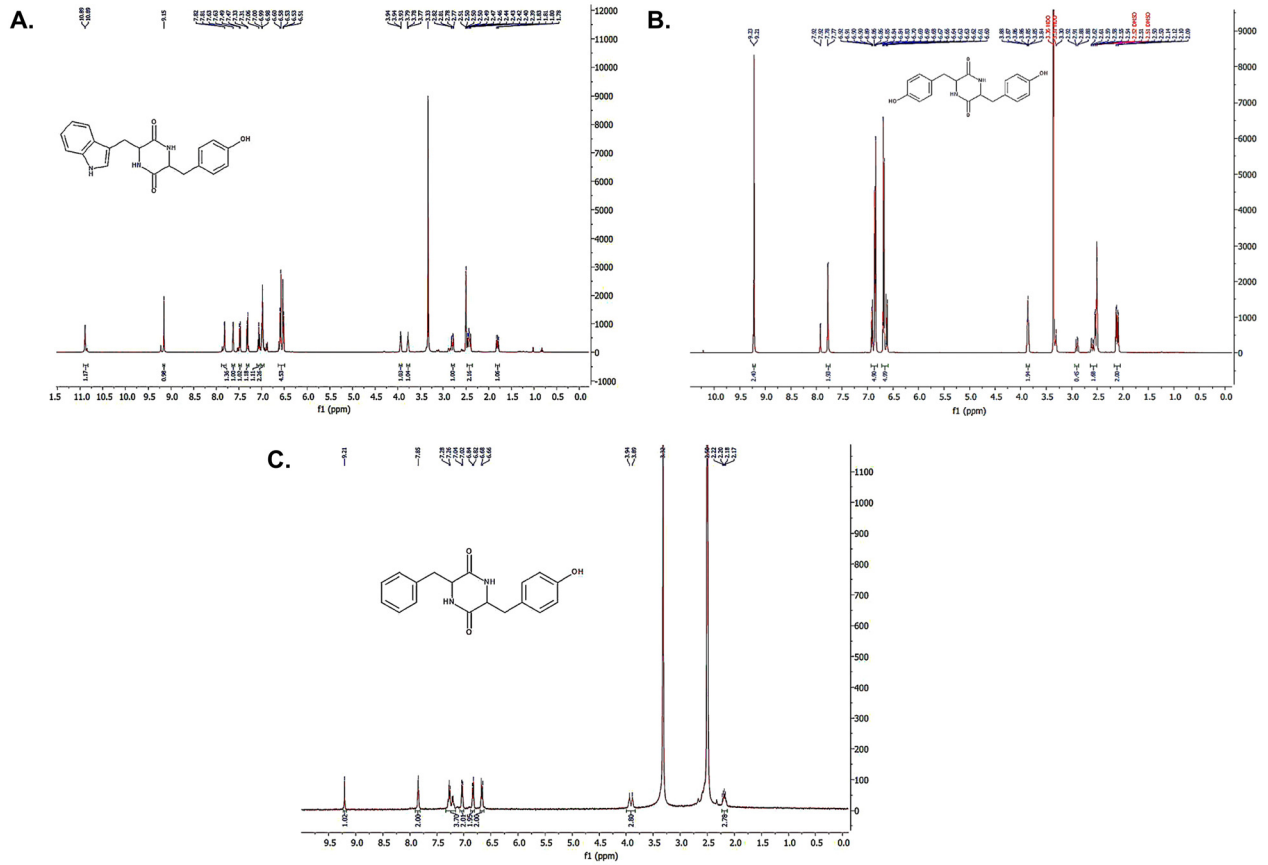

Fig. 8 ^{1}HNMR spectra of WY (A), YY (B), and FY (C) PECVD-deposited peptide nanostructures in DMSO-d^{6}.

facilitates intermolecular crosslinking reactions, resulting in highly cross-linked three-dimensional network structures in the deposited films.

Thermal characterization using DSC and TGA instrumentation indicated that the amount of heat required for the sublimation of peptides onto the cold substrate placed above was monomer-specific and varied depending on the amino acid sequence of each peptide. Cyclization of dipeptides as demonstrated by the LC-MS data leads to structural rigidity as well as stability crucial to the self-assembly process. The degree of freedom in the peptide chain is reduced due to cyclization, and these geometrical constraints promote intermolecular interactions such as π–π stacking and hydrogen bonding, essential for the formation of stable supramolecular structures. π–π stacking also contributes to the stabilization of the α-helical structures observed in the deposited nanostructures. The formation of diketopiperazine ring due to cyclization, when compared to the linear monomer which has a single amide bond and a free amine group, contributes to the stronger interactions[54–57]

SEM demonstrated the formation of morphologically unique aggregate structures under variable deposition parameters, namely, chamber pressure, radio frequency (RF) power, argon flow rate, deposition time, tilt of the substrate, height of deposition, presence of physical constraints, and the amount of peptide. The peptide monomers preferentially assembled into arrays of vertically aligned nanostructures. The formation of distinct peptide nanostructures, particularly nanotubes and nanoflowers, under varying PECVD parameters is influenced by monomer mobility, nucleation density, and the presence of physical constraints. When the sublimation of peptide monomers is relatively unrestricted and nucleation sites are limited, the monomers preferentially stack and align forming elongated nanorods/tubes.[58] Conversely, higher chamber pressures, extended deposition times and physical confinement on the substrate, produce a heightened multidirectional nucleation and outward growth, producing splayed hierarchical nanoflower morphologies. Elevated pressures (~0.08 Torr) combined with longer deposition times (≥ 15 min) promoted the formation of clustered, flower-like structures. We hypothesized that monomer mobility increases the likelihood of gas-phase molecular collisions and enhances the nucleation density in the focused regions of the substrate, which encourages branching. In contrast, rod- and tube-like morphologies were favored under lower pressure conditions (0.0002 Torr) and moderate deposition times (~10 min). A longer average time between gas-phase molecular collisions enables slower and more directional growth along the axial direction. These conditions suppress excessive multidirectional nucleation, resulting in straighter and more uniform nanorods/tubes.[59] The application of constraints, such as TEM grids or metallic meshes, alters the molecular alignment by imposing topographical limitations that restrict continuous thin-film formation and rotational freedom at the substrate. These constraints

favor multidirectional nucleation owing to the high concentration of peptide monomers near the edges and junctions of the mesh grids, contributing to shifts in the electrostatic interactions.[60] To assess the molecular interactions dictating these assemblies, secondary structure changes following deposition were observed using NMR, FTIR, Raman spectroscopy, XRD, WCA, and CD spectroscopy. Comparison of the peptides before and after deposition revealed cyclization events that favored the formation of α-helical-like secondary structures in the PECVD nanostructures due to localized ordering. Furthermore, the samples were highly crystalline and exhibited hydrophobic properties that were consistent with the corresponding peptide side chains. This confirmed that although the intrinsic chemical makeup of the peptides was not altered, the structural orientation and monomer interactions were modified during deposition.

Because peptides exhibit stability, robust mechanical strength, biocompatibility, and sequence specificity, we foresee the utilization of these bioactive coatings in a number of fields, including catalysis, regenerative medicine, molecular sensing, bioelectronics, drug delivery, and even biological imaging.[14,61] One application we intend to explore is the use of these scaffolds to stimulate neural cell attachment, proliferation, and differentiation. Currently, neurons in the central nervous system do not regenerate after axonal disconnections due to injury or disease. This is primarily due to the significant presence of growth-inhibiting molecules in the immediate extracellular environment, as well as cell-autonomous failure to upregulate genes associated with growth and survival.[62] Owing to our ability to manipulate the complexity of microscopic and nanoscale topographical features, we can design scaffolds that exhibit an increase in functional cues that contribute to the gradual polarization of neural cells. Further studies are required to determine the appropriate combinations of deposition conditions and amino acid sequences to maximize the outcomes of PECVD-deposited scaffolds for specific, targeted biomedical applications.

4. Experimental section

4.1. Substrate preparation

Silicon wafers and glass slides were used as substrates for PECVD. These were initially cleaned using the RCA method (originally developed for the Radio Corporation of America). The substrates were stored in ultrapure water until use. For proper adhesion of peptide deposition, these substrates were further treated with aminosilane to provide amine groups as coupling agents on the silica-based surfaces for functionalization. A 5% solution of aminosilane in methanol was used to coat the substrates. After treatment, they were washed and cleaned ultrasonically in the following sequence: acetone (10–15 min), methanol (2–5 min), and DI water (rinse). These were finally dried using nitrogen gas prior to deposition.

4.2. Vapor deposition

Pre-cleaned glass coverslips/silicon wafers were attached to the substrate holder, which was held at a specific distance from the crucible containing the required amount of peptide. Tryptophan–tyrosine (WY), dityrosine (YY), and phenylalanine–tyrosine (FY) peptides were purchased from Bachem (Switzerland). If the deposition involved confinement, the substrate was prepared using a metal mesh with selected gaps, that is, several hundred microns to millimeters. The chamber was then closed to achieve a high vacuum, and an in-house built system (SI Fig. 1) used two pumps: a rough vacuum pump and a turbo pump. The set point for the pressure was controlled using a butterfly valve built into the system. Ultrapure argon was piped into the chamber using flow controllers to control the flow rate (5–20 sccm). A radio frequency (RF) power source from Seren was used for plasma generation. Various parameters, such as RF power, frequency (Hz), pulsation, DC%, argon flow rate (sccm), pressure set point, heat, and exposure time, were selected for a particular deposition. The temperature setting for deposition was primarily dependent on the glass-liquid transition phase temperature obtained by conducting dynamic thermal behavior analysis of monomers using differential scanning calorimetry (DSC) and thermogravimetric analysis (TGA).

4.3. Thermal characterization

Differential scanning calorimetry (DSC) Q1000 (TA Instruments, New Castle, DE, USA) equipped with an autosampler, digital mass flow controller, and chromel/constantan Tzero thermocouple was used to observe the thermodynamic behavior of the peptide monomers to elucidate the factors determining protein folding and stability. To determine the cyclization and melting points of the peptides, energy shifts were recorded at temperatures ranging from 0 to 400 °C. Each sample was subjected to a slow ramp of 5 °C min^{-1} (nitrogen purge flow rate of 50 mL min^{-1}). Thermogravimetric analysis with a TGA/Q500 device was performed on the samples. The experiment was performed under the same conditions as those used for DSC measurements. The onset temperature of the glass-liquid transition and decomposition (T_d, °C) were recorded.

4.4. Morphological characterization

To study the morphological characteristics of the PECVD peptide depositions, imaging was performed using a scanning electron microscope (Hitachi SU-5000) with an accelerating voltage range of 0.5–10 kV. The samples were sputter-coated with 4 nm gold before imaging.

4.5. High performance liquid chromatography (HPLC)

Chromatographic separation was performed using a Shimadzu Prominence-i-LC-2030 HPLC system equipped with a Shimadzu RF-20A fluorescence detector. PECVD-deposited peptide nanostructures and their corresponding monomers were solubilized in HPLC-grade acetonitrile and centrifuged at full speed for 5 min to eliminate any undissolved samples before analysis. The HPLC column was a Shimadzu C-18, 3.0 × 75.0 mm, 5 μm particle size LC column, and the flow rate employed through the column was 0.200 mL min^{-1} at a temperature of 40 °C. Following an initial 15-minute equilibration period with mobile phase A (95 : 5 water with 0.1% trifluoroacetic acid: acetonitrile), linear gradient

separation was performed for a further 15 min, transitioning from to 0–100%, mobile phase B (95 : 5 acetonitrile: water with 0.1% trifluoroacetic acid). The eluents were measured by UV absorption at a detection wavelength of 280 nm (WY, YY, and FY), and the retention peaks were recorded using the LabSolutions software.

4.6. Spectroscopy

Infrared spectra were obtained using an Agilent Cary 630 Attenuated Total Reflectance (ATR) spectrometer in the range–400–4000 cm^{-1}. The absorbance readings were recorded in triplicate, averaged, and downloaded for further analyses. Spectra were obtained at an average of 100 scans (resolution of 2 cm^{-1}) at a speed of 2.5 kHz. Raman spectra of the WY, YY, and FY PECVD nanostructures were collected using a WITec alpha 300 M confocal Raman system within the range of 400 cm^{-1} to 3600 cm^{-1}. For the Raman spectra, a minimum of five acquisitions with an integration time of 4 s were averaged.

4.7. Circular dichroism (CD)

CD analysis of the WY, YY, and FY PECVD nanostructures was performed using a J-810 spectropolarimeter (Jasco, Inc., Tokyo, Japan), averaged over three scans with a range of 190–300 nm and a speed of 20 nm min^{-1}. Stock solutions of nanostructures were diluted in double-distilled water to a final concentration range of 0.025–0.125 mg mL^{-1}. The spectral data were processed using the Contin-LL and K2D methods available in DichroWeb.

4.8. Water contact angle (WCA) measurement

Static water contact angle (WCA) measurements were performed to assess the surface wettability of the WY, YY, and FY PECVD-deposited nanostructures. WCA measurements were conducted using the sessile drop method on a Ramé-Hart goniometer (Model 90-U3-PRO, Ramé-Hart Instrument Co.) with a precision of $\pm 0.1^{\circ}$. A droplet of deionized water was gently placed on the PECVD nanostructures deposited on glass coverslips under ambient conditions, and the contact angles were recorded within 5 s after deposition. The measurements were performed in triplicate at independent surface locations for each sample across three samples, and the values were averaged.

4.9. X-ray diffraction (XRD)

X-ray powder diffraction (XRD) spectra of the WY, YY, and FY PECVD nanostructures and monomers were recorded using a Rigaku Miniflex 600 theta:2-theta diffractometer to analyze the elemental composition. The deposited samples were carefully collected, ground, and transferred into a 0.5 mm depth XRD sample holder for analysis. The scan parameters include a 5–40 2-theta scan range with a step size of 0.005 2-theta and a count time of 5.0 s per step.

4.10. Nuclear magnetic resonance

The dipeptide monomers and their corresponding PECVD-deposited nanostructures were dissolved in deuterated DMSO at a concentration of 10 mg mL^{-1} and loaded onto a Bruker AVANCE III HD 400 MHz High-Performance Digital NMR for their respective 1H spectra. Chemical shifts were analyzed using the MestReNova package, and the structures were drawn using ChemDraw software.

Author contributions

MV: conceptualization, methodology. JP and PM: data curation, visualization, writing – original draft preparation. JP, PM, and MN: investigation. MV: supervision. JP: software, validation. JP, PM, and MV: writing, reviewing, and editing.

Conflicts of interest

The authors declare that they have no conflicts of interest.

Data availability

The data generated in this study are included in this published journal article and the supplementary information (SI) files. Supplementary information: figures, table of deposition conditions, LC-MS and NMR data. See DOI: https://doi.org/10.1039/d5ma01273b.

The raw data supporting the findings of this study are available from the corresponding author, upon request.

Acknowledgements

This work was supported by the U.S. Department of Defense NDEP program through a cooperative agreement with the Natick Soldier Research, Development and Engineering Center (Award Number W911QY2320002). We acknowledge the support of Dylan Bryda, a graduate bioengineering student, for his contribution to the sample synthesis. The electron microscopy images in this study were obtained using a scanning electron microscope supported by the National Science Foundation under grant no. 1726239. The CD spectrometer used in this study was supported by the National Institute of General Medical Sciences of the National Institutes of Health under the Award Number S10GM154301. For our material characterization efforts, we are grateful to Md. Sagir Mia of the Chemistry Department at UMass Dartmouth for his assistance in obtaining LC-MS data. We also acknowledge Jessica Davis and the Geological Sciences Department at Bridgewater State University for the use of their XRD facilities.

References

1 A. Levin, T. A. Hakala, L. Schnaider, G. J. L. Bernardes, E. Gazit and T. P. J. Knowles, *Nat. Rev. Chem.*, 2020, **4**, 615–634.
2 T. Li, X.-M. Lu, M.-R. Zhang, K. Hu and Z. Li, *Bioact. Mater.*, 2022, **11**, 268–282.
3 K. Tao, P. Makam, R. Aizen and E. Gazit, *Science*, 2017, **358**(6365), eaam9756.
4 S. H. Kim and J. R. Parquette, *Nanoscale*, 2012, **4**, 6940–6947.

5 S. Chakraborty, K. el Battioui and T. Beke-Somfai, *Small Science*, 2024, **4**, 2300217.
6 M. C. Vasudev, H. Koerner, K. M. Singh, B. P. Partlow, D. L. Kaplan, E. Gazit, T. J. Bunning and R. R. Naik, *Biomacromolecules*, 2014, **15**, 533–540.
7 S. Jain, A. John, C. E. George and R. P. Johnson, *Biomacromolecules*, 2023, **24**, 531–565.
8 J. J. Warren, J. R. Winkler and H. B. Gray, *FEBS Lett.*, 2012, **586**, 596–602.
9 H. Lee, H.-S. Jang, D.-H. Cho, J. Lee, B. Seong, G. Kang, Y.-S. Park, K. T. Nam, Y.-S. Lee and D. Byun, *ACS Nano*, 2020, **14**, 1738–1744.
10 Y. Tan, R. Y. Adhikari, N. S. Malvankar, S. Pi, J. E. Ward, T. L. Woodard, K. P. Nevin, Q. Xia, M. T. Tuominen and D. R. Lovley, *Small*, 2016, **12**, 4481–4485.
11 J. H. Yoon, M.-K. Song, W. Ham, K. J. Park, J.-M. Park, S. D. Namgung and J.-Y. Kwon, *Adv. Funct. Mater.*, 2025, **35**, 2415222.
12 B. Beyazay, H. Çelik, Y. Yücel, M. Özdemir, E. Çalışkan, K. Koran and F. Biryan, *ACS Omega*, 2025, **10**, 8588–8600.
13 K.-H. Dahmen, *Encyclopedia of Physical Science and Technology*, ed. R. A. Meyers, Academic Press, New York, 3rd edn, 2003, pp. 787–808, DOI: 10.1016/B0-12-227410-5/00102-2.
14 L. Sun, G. Yuan, L. Gao, J. Yang, M. Chhowalla, M. H. Gharahcheshmeh, K. K. Gleason, Y. S. Choi, B. H. Hong and Z. Liu, *Nat. Rev. Methods Primers*, 2021, **1**, 5.
15 N. Chen, D. H. Kim, P. Kovacik, H. Sojoudi, M. Wang and K. K. Gleason, *Annu. Rev. Chem. Biomol. Eng.*, 2016, **7**, 373–393.
16 B. Schurink, W. T. E. van den Beld, R. M. Tiggelaar, R. W. E. van de Kruijs and F. Bijkerk, *Coatings*, 2022, **12**, 685.
17 A. Khlyustova, Y. Cheng and R. Yang, *J. Mater. Chem. B*, 2020, **8**, 6588–6609.
18 M. C. Vasudev, K. D. Anderson, T. J. Bunning, V. V. Tsukruk and R. R. Naik, *ACS Appl. Mater. Interfaces*, 2013, **5**, 3983–3994.
19 B. R. Coad, P. Favia, K. Vasilev and H. J. Griesser, *Plasma Processes Polym.*, 2022, **19**, 2200121.
20 C. M. Didier, D. Fox, K. J. Pollard, A. Baksh, N. R. Iyer, A. Bosak, Y. Y. Li Sip, J. F. Orrico, A. Kundu, R. S. Ashton, L. Zhai, M. J. Moore and S. Rajaraman, *ACS Appl. Mater. Interfaces*, 2023, **15**, 37157–37173.
21 A. Loesch-Zhang, A. Geissler and M. Biesalski, *Plasma Processes Polym.*, 2023, **20**, e2300016.
22 S. Bonot, R. Mauchauffé, N. D. Boscher, M. Moreno-Couranjou, H. M. Cauchie and P. Choquet, *Adv. Mater. Interfaces*, 2015, **2**, e1800121.
23 J. Kousal, J. Sedlaříková, Z. Rašková, Z. Krtouš, L. Kučerová, A. Hurajová, M. Vaidulych, J. Hanuš and M. Lehocký, *Polymers*, 2020, **12**, 1263.
24 V. A. Adhav and K. Saikrishnan, *ACS Omega*, 2023, **8**, 22268–22284.
25 M. Vasudev, Y. Hamedani, P. Macha, T. J. Bunning and R. R. Naik, Plasma-Enhanced Chemical Vapor Deposition: Where we are and the Outlook for the Future, in *Chemical Vapor Deposition – Recent Advances and Applications in Optical, Solar Cells and Solid State Devices*, ed. S. Neralla, IntechOpen, 2016, DOI: 10.5772/64654.
26 A. Choukourov, H. Biederman, D. Slavinska, L. Hanley, A. Grinevich, H. Boldyryeva and A. Mackova, *J. Phys. Chem. B*, 2005, **109**, 23086–23095.
27 I. Levchenko, S. Xu, O. Baranov, O. Bazaka, E. P. Ivanova and K. Bazaka, *Molecules*, 2021, **26**, 4091.
28 H. K. Yasuda, *Plasma Processes Polym.*, 2005, **2**, 293–304.
29 P. Singh, R. K. Sharma, O. P. Katare and N. Wangoo, *Mater. Adv.*, 2022, **3**, 6518–6528.
30 B. Bank-Srour, P. Becker, L. Krasovitsky, A. Gladkikh, Y. Rosenberg, Z. Barkay and G. Rosenman, *Polym. J.*, 2013, **45**, 494–503.
31 M. R. Amirzada, A. Tatzel, V. Viereck and H. Hillmer, *Appl. Nanosci.*, 2015, **6**, 215–222.
32 P. Shende, P. Kasture and R. S. Gaud, *Artif. Cells, Nanomed., Biotechnol.*, 2018, **46**, 413–422.
33 Y. Liu, X. Ji and Z. He, *Nanoscale*, 2019, **11**, 17179–17194.
34 Y. Ni, Z. Sun, Z. Zeng, F. Liu and J. Qin, *New J. Chem.*, 2019, **43**, 18629–18636.
35 Y. Su, X. Yan, A. Wang, J. Fei, Y. Cui, Q. He and J. Li, *J. Mater. Chem.*, 2010, **20**, 6734–6740.
36 M. Sakurai, P. Koley and M. Aono, *Chem. Commun.*, 2014, **50**, 12556–12559.
37 S. Fleming, P. W. J. M. Frederix, I. Ramos Sasselli, N. T. Hunt, R. V. Ulijn and T. Tuttle, *Langmuir*, 2013, **29**, 9510–9515.
38 M. Hughes, P. W. J. M. Frederix, J. Raeburn, L. S. Birchall, J. Sadownik, F. C. Coomer, I. H. Lin, E. J. Cussen, N. T. Hunt, T. Tuttle, S. J. Webb, D. J. Adams and R. V. Ulijn, *Soft Matter*, 2012, **8**, 5595–5602.
39 A. Sadat and I. J. Joye, *Appl. Sci.*, 2020, 5918.
40 P. Macha, L. Perreault, Y. Hamedani, M. L. Mayes and M. C. Vasudev, *ACS Appl. Biomater.*, 2018, **1**, 1266–1275.
41 F. Adar, *Spectroscopy*, 2022, **37**, 9–13.
42 A. Miles, S. Ramalli and B. Wallace, *Protein Sci.*, 2021, **31**, 37–46.
43 L. Whitmore and B. Wallace, *Nucleic Acids Res.*, 2004, **32**, W668–W673.
44 L. Whitmore and B. Wallace, *Biopolymers*, 2007, **89**, 392–400.
45 M. A. Andrade, P. Chacón, J. Merelo and F. Morán, *Protein Eng., Des. Sel.*, 1993, **6**, 383–390.
46 S. Provencher and J. Gloeckner, *Biochemistry*, 1981, **20**, 33–37.
47 I. van Stokkum, H. Spoelder, M. Bloemendal, R. van Grondelle and F. Groen, *Anal. Biochem.*, 1990, **191**, 110–118.
48 M.-I. Aguilar and A. W. Purcell, *Encyclopedia of Analytical Science*, Elsevier Ltd., 2 edn, 2005, pp. 29–36.
49 I. León, E. R. Alonso, C. Cabezas, S. Mata and J. L. Alonso, *Commun. Chem.*, 2019, **2**, 3.
50 H. Zhang, S. Lou and Z. Yu, *Langmuir*, 2019, **35**, 4710–4717.
51 B. A. Nerger, K. Kashyap, B. T. Deveney, J. Lou, B. F. Hanan, Q. Liu, A. Khalil, T. Lungjangwa, M. Cheriyan, A. Gupta, R. Jaenisch, D. A. Weitz, L. Mahadevan and D. J. Mooney, *Proc. Natl. Acad. Sci. U. S. A.*, 2024, **121**, e2410806121.
52 K. M. Makwana and R. Mahalakshmi, *Protein Sci.*, 2015, **24**, 1920–1933.

53 L. Mengmeng, S. Dan, W. Ping, W. Danying, Z. Yidi, L. Mingqiang, Z. Jinghui and Z. Yanmin, *RCS Adv.*, 2016, **6**, 82688–82697.
54 L. Adler-Abramovich, M. Reches, V. L. Sedman, S. Allen, S. J. B. Tendler and E. Gazit, *Langmuir*, 2006, **22**, 1313–1320.
55 T. Li, X.-M. Lu, M.-R. Zhang, K. Hu and Z. Li, *Bioact. Mater.*, 2021, **11**, 268–282.
56 X. Zhu, R. Duan, S. Y. Chan, L. Han, H. Liu and B. Sun, *J. Adv. Res.*, 2022, **43**, 27–44.
57 Q. Song, Z. Cheng, M. Kariuki, S. C. L. Hall, S. K. Hill, J. Y. Rho and S. Perrier, *Chem. Rev. J.*, 2021, **121**, 13936–13995.
58 K. Ostrikov, I. Levchenko, U. Cvelbar, M. Sunkara and M. Mozetic, *Nanoscale*, 2010, **2**, 2012–2027.
59 H. Hamidinezhad, Y. Wahab, Z. Othaman and A. Khamim Ismail, *J. Cryst. Growth.*, 2011, **332**, 7–11.
60 C. Yuan, Q. Li, R. Xing, J. Li and X. Yan, *Chemistry*, 2023, **9**, 2425–2445.
61 L. Wang, N. Wang, W. Zhang, X. Cheng, Z. Yan, G. Shao, X. Wang, R. Wang and C. Fu, *Signal Transduction Targeted Ther.*, 2022, **7**(1), 48.
62 E. A. Huebner and S. M. Strittmatter, *Results Probl. Cell Differ.*, 2009, **48**, 339–351.